IEEE Access
Multidisciplinary | Rapid Review | Open Access Journal

Received April 25, 2022, accepted May 3, 2022, date of publication May 9, 2022, date of current version May 19, 2022.

Digital Object Identifier 10.1109/ACCESS.2022.3173616

A Ring-Connected Dual Active Bridge Based DC-DC Multiport Converter for EV Fast-Charging Stations

YOUSEF NAZIH[1], MOHAMED G. ABDEL-MONEIM[1], AHMED A. ABOUSHADY[2], (Senior Member, IEEE), AYMAN S. ABDEL-KHALIK[1], (Senior Member, IEEE), AND MOSTAFA S. HAMAD[3], (Senior Member, IEEE)

[1]Department of Electrical Engineering, Alexandria University, Alexandria 21544, Egypt
[2]Department of Electrical and Electronic Engineering, Glasgow Caledonian University, Glasgow G4 0BA, U.K.
[3]Research and Development Center, Arab Academy for Science, Technology and Maritime Transport, Alexandria 21568, Egypt

Corresponding author: Yousef Nazih (yousef.nazih@alexu.edu.eg)

ABSTRACT This paper proposes a multiport DC-DC converter for EV fast-charging stations. The proposed converter is comprised of Ring-Connected Dual Active Bridge (RCDAB) DC-DC converters, where the connection point between every two adjacent DABs provides a DC port. Bypass switches are added to each DAB to eliminate unnecessary power processing stages in the event of idle ports (no EVs) (open circuit ports). The nature of the ring connection of the RCDAB theoretically allows infinite internal power flow solutions within the ring to satisfy a certain power flow scenario at the DC ports, hence, the optimal power flow solution can be selected to minimize total RMS current and losses. Single-phase shift control is applied to this optimization problem to make it simple. A novel closed-loop control scheme using Bisection optimization is developed to minimize the total RMS current. A control-hardware-in-the-loop (CHiL) validation is carried out for a 5-port network of the proposed topology to investigate the converter efficiency and fault tolerance/availability characteristics. Also, an experimental hardware validation is implemented for a 3-port network where different scenarios for power flow and faults are performed. Finally, a comparative discussion between the proposed topology and other multiport topologies in literature is presented revealing the superior performance of the RCDAB topology.

INDEX TERMS Dual active bridge (DAB), DC-DC multiport converter, electric vehicle (EV), fast charging, ring-connected DAB (RCDAB), single phase shift (SPS) control.

I. INTRODUCTION

Electric vehicle (EV) market has been growing extensively all over the world due to its promising advantages of high energy efficiencies and environmentally friendly performance due to zero emissions and the remarkable drop in its price. Therefore, the need for charging stations is increased to meet the growing number of EVs. Some EV charging stations have renewable energy sources as well as energy storage systems integrated into them [1]. EV charging stations are classified into several levels according to the charging speed. The first category is level 1 (slow) AC charging, which can take place in residential areas. However, level 2 AC charging (semi-fast), which requires a 240 V outlet, is considered as the primary method for implementation in most private and public facilities [2]. Level 1 and 2 charging usually utilizes a single-phase approach. On the other hand, Level 3 AC charging and DC fast charging use a three-phase approach and are implemented in commercial applications [3]. In literature, [4], [5] provide the standards for the technical specifications that are used in designing DC electric vehicle chargers. Moreover, the EV battery chargers can be either on-board or off-board, where onboard chargers have limited power capability due to cost, weight, and volume constraints [6]. Also, EV battery chargers can provide either unidirectional or bidirectional power flow.

Most existing topologies in EV chargers, which are based on DC-DC converters, are two port-based chargers [7], where individual power converters can be used to control the power

The associate editor coordinating the review of this manuscript and approving it for publication was Chi-Seng Lam.

flow among multiple sources in addition to the energy storage devices and EVs. However, multiport converters are better candidates for this application because multiport topologies utilize a lower number of components and, hence, achieve lower cost and higher power density compared to traditional systems that use individual power converters [8], [9].

Various multiport topologies have been reported in the literature, where each of them has its pros and cons. Non-isolated multiport topologies are the most common topologies for low power applications and low-to-medium voltage stepping ratios [9]. Non-isolated multiport converters consist of different combinations of basic converter cells like a buck, boost, and/or buck-boost [10]–[13]. Others combine half-bridge and full-bridge converters to form non-isolated multiport converters [14], [15]. In addition, In [16], a multiple-input power converter (MIPC) is proposed, which is composed of multiple-legs inverter so that each leg can be connected to a different port. It provides low switch count; however, it cannot tolerate DC faults. Other groups of non-isolated multiport topologies use simpler construction of one or two basic converters such as buck or boost or other non-isolated converters but require relays or low switching devices to reconfigure the power flow between multiple ports [17]–[19]. Therefore, these topologies have an overall low operational flexibility. Other converters have limited power flow capability, where the converter can provide bidirectional power flow between specific ports such as the non-isolated three-port converter (NITPC) in [20] and the fully soft-switched multiport converter (FSSMPC) in [12]. A multiport LCL DC Hub-based converter is proposed in [21], which can limit the DC fault current and reduce the circulating reactive power. However, this topology provides no galvanic isolation between the ports and utilizes large count of passive elements.

On the other hand, many isolated multiport topologies are found in the literature that vary depending on the structure of the isolating transformer. Some topologies are based on a single two-winding transformer to develop an isolated multiport converter [22], [23], where one or more ports are combined at either the primary or the secondary sides of the transformer. Besides, in [24] and [25] a three-port converter is introduced that is based on an interleaved-boost full-bridge converter (IBFBC). The switches are driven by pulse width modulation signals, where the duty cycle controls the power flow between the two input ports, while the output voltage is regulated by the phase shift angle. However, these topologies do not provide isolation between all ports.

Nevertheless, other isolated multiport topologies are based on two or more two-winding transformer-coupled together to provide isolation and power flow between the ports, as in [26] and [27]. Alternatively, the multi-winding transformer has been widely used in multiport topologies [28] that consists of half-bridge [29] or full-bridge [30]–[34] DC to AC and AC to DC conversion stages allowing for a bi-directional power flow. The main difference between the half-bridge and full-bridge-based converters is that in the half-bridge-based converter, only square wave voltage waveform can be generated, hence duty ratio control cannot be applied resulting in a narrow soft-switching range. On some occasions [35], one of the ports is based on unidirectional series resonant topology, where it is comprised of a resonant tank and a full bridge of diodes to allow for a higher power flow. In [36], a multi-winding transformer-based LLC resonant converter (LLC-MWT) is proposed, which can provide soft-switching capability although it cannot tolerate open circuit faults. Moreover, a multi-winding transformer converter based on multiple-active-bridge (MAB-MWT) is discussed in [32], where it provides bidirectional power flow at all ports. However, it lacks modularity (ability to extend the number of ports) and cannot tolerate open circuit faults in the H-bridges.

In this paper, a ring-connected DAB (RCDAB)-based DC-DC bidirectional multiport converter is proposed that is intended for electric vehicles fast-charging stations. The proposed RCDAB topology consists of multi-DABs coupled in a ring shape where the connection point between every two adjacent DABs provides a DC port outlet. Also, bypass switches are added to each DAB to eliminate any unnecessary power processing stages in case there are idle ports (no supply or battery is connected to the port). The RCDAB topology theoretically offers an infinite number of internal power flow possibilities for a given power flow scenario at the DC ports, thus a control algorithm is provided to ensure operation at the optimum point where minimum total RMS current is achieved.

The main advantages of the proposed RCDAB topology over other existing topologies in literature are summarized as follows:

- The ring connection in the RCDAB topology provides an extra degree of freedom with a theoretically infinite number of solutions for a given desired power flow requirement at the DC ports using the simple single-phase shift (SPS) control. Hence an optimum point can be obtained that achieves minimum current with minimized losses. This cannot be achieved with other non-ring multiport converters using the same SPS control where only single non-optimal solutions exist.
- Fully modular with a standard DAB circuit being the main unit, in addition to ease of scalability.
- Higher availability/fault tolerance particularly to open circuit failures due to the ring structure providing an alternative power route to any particular DC port.

The rest of the paper is organized as follows: Section II discusses the DAB with detailed mathematical analysis for the active power flow and RMS current calculations. Section III provides a detailed explanation and mathematical analysis for the RCDAB topology in addition to a closed-loop control algorithm to determine the optimum operating point for each DAB. Section IV provides steady state analysis in the form of loss analysis and power flow capability of the RCDAB topology. In Section V, a control-hardware-in-the-loop (CHiL) validation is implemented for the proposed

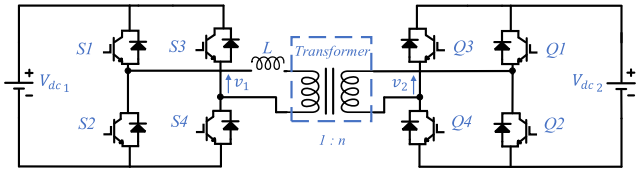

FIGURE 1. The exact configuration of dual active bridge.

RCDAB topology discussing different scenarios of normal operation and port/converter faults. Moreover, experimental validation, using a laboratory prototype of a 3-port network, is constructed for the proposed topology which is provided in Section VI. Finally, in section VII, a discussion is provided to evaluate the RCDAB topology when compared to different multiport DC-DC topologies.

II. DUAL ACTIVE BRIDGE CIRCUIT ANALYSIS

DAB circuit analysis and modulation techniques are widely explained in literature [37], [38]. A brief summary of this circuit analysis is introduced to highlight the basis of the RCDAB topology. FIGURE 1 shows the DAB exact configuration, consisting of two H-bridges located at both sides of a medium/high-frequency transformer. The main function of the transformer is to provide isolation and voltage matching between the low and high voltage buses. In addition, the leakage inductance of the transformer acts as an instantaneous energy storage element, which can be increased by adding an auxiliary series inductor.

The power flow between the two sides of a DAB is controlled by regulating the phase shift between the square voltage generated by each of the H-bridges. The simplest modulation principle is illustrated in FIGURE 2, where each H-bridge generates a square wave voltage with all semiconductor devices operating at 50% duty cycle, and only phase difference between both H-bridges is changed to control the power flow. This modulation method is adopted in this paper and is well known as the single-phase shift (SPS) method.

Using fundamental harmonic analysis, DAB equivalent circuit is depicted in FIGURE 3, where each side of the DAB is replaced by a fundamental AC source. The RMS phasor of the fundamental voltage component at both sides (1 and 2) $\bar{V}_1$ and $\bar{V}_2$ can be represented as in (1) and (2), respectively.

$$\bar{V}_1 = \frac{2\sqrt{2}}{\pi} V_{dc_1} \angle 0 \tag{1}$$

$$\bar{V}_2 = \frac{2\sqrt{2}}{\pi} V_{dc_2} \angle -\delta \tag{2}$$

where V_{dc_1} and V_{dc_2} are the DC voltage levels of sides (1) and (2), respectively, and δ is the phase difference between the two AC voltages. The inductance (L) in FIGURE 3 represents the total of transformer leakage inductance and any auxiliary inductance.

Since n represents the turn ratio between sides (2) and (1), then, the power transferred between both sides, assuming

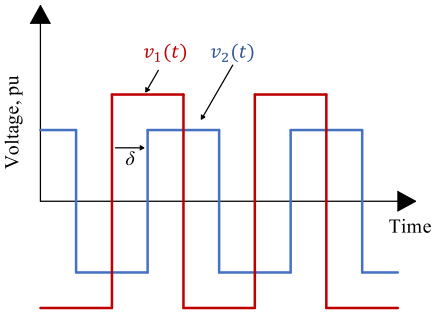

FIGURE 2. Single-phase shift (SPS) modulation technique.

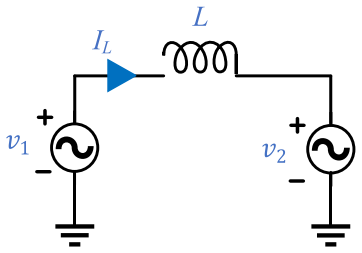

FIGURE 3. DAB fundamental harmonic analysis equivalent circuit.

lossless DAB, is calculated as in (3).

$$P_{DAB} = \frac{V_1 V_2'}{2\pi f_s L} sin\,(\delta) \tag{3}$$

where V_2' is the AC RMS voltage of the fundamental voltage component at the side (2) referred to side (1).

$$V_2' = \frac{V_2}{n} \tag{4}$$

Assume that the base values are as follows:

$$P_{base} = \frac{V_{base}^2}{2\pi f_s L_{base}} \tag{5}$$

$$Z_{base} = X_l = 2\pi f_s L_{base} \tag{6}$$

$$I_{base} = \frac{V_{base}}{X_l} = \frac{V_{base}}{2\pi f_s L_{base}} \tag{7}$$

Then the per-unit value of the power at side (1) can be represented as follows, assuming that the AC inductance $L = L_{base}$.

$$P_{DAB_{pu}} = \frac{V_1 V_2'}{V_{base}^2} sin\,(\delta) = V_{1_{pu}} V_{2_{pu}}' sin\,(\delta) \tag{8}$$

The current i_L is given by;

$$\bar{I}_L = \frac{\bar{V}_1 - \bar{V}_2'}{jX_l} = \frac{V_2' \sin(\delta) - j(V_1 - V_2' \cos(\delta))}{X_l} \tag{9}$$

Then the RMS per-unit value of the current is calculated as follows:

$$\bar{I}_{L_{pu}} = V_{2_{pu}} \sin(\delta) - j(V_{1_{pu}} - V_{2_{pu}} \cos(\delta)) \tag{10}$$

III. THE PROPOSED RCDAB-BASED DC-DC MULTIPORT CONVERTER

A. RCDAB TOPOLOGY

The RCDAB converter consists of multi-DABs connected back-to-back in a ring shape as shown in FIGURE 4, where the connection between every two adjacent DABs provides a DC port outlet. Each DAB can be bypassed using two bypass switches shown in FIGURE 4. The converter is comprised of N DABs and N DC ports. A reference direction for power flow through each DAB is assumed to be in a clockwise direction. For each port positive power is assumed to be injected and negative power is absorbed. The power flow to/from each port P_i is controlled only by the two adjacent DABs as in (11).

$$P_i = P_{DAB_{i+1}} - P_{DAB_i} \tag{11}$$

where P_i is the power of port i. It is clear that the maximum power flow to/from each port depends on the maximum power flow through each of the two adjacent DABs. Substituting by (8) in (11) with considering the ports numbering, then the power of each port can be given by;

$$P_{i_{pu}} = V_{i_{pu}} V_{i+1_{pu}} \sin(\delta_{i+1}) - V_{i_{pu}} V_{i-1_{pu}} \sin(\delta_i) \tag{12}$$

where $V_{i_{pu}}$ is the per-unit AC RMS voltage at port (i) side, while δ_i is the phase difference between the two AC voltages of DAB (i). It is worth noting that $i = 1, ..N$, where if $i = 1$, then $i - 1 = N$, and if $i = N$, then $i + 1 = 1$.

It is worth noting that the converter losses are neglected in the mathematical analysis for simplification of the controller derivation. Therefore, the summation of the powers at all ports must be equal to zero as follows:

$$\sum_{i=1}^{N} P_i = 0 \tag{13}$$

Then the power equations of only N-1 ports are independent with N controllable variables (phase shift angles of the N DABs). Therefore, there is a wide range of solutions to the power flow problem. Hence, an additional constraint to minimize the total RMS current is added to locate the optimum operating point which provides the lowest losses.

The square of the total per-unit RMS current of the RCDAB converter is calculated as follows:

$$I^2_{L_{pu_{total}}} = \sum_{i=1}^{N} I^2_{L_{pu_i}} \tag{14}$$

Substituting with (10) in (14) yields:

$$I^2_{L_{pu_{total}}} = 2\sum_{i=1}^{i=N} {V_{i_{pu}}}^2 - 2\sum_{i=2}^{i=N} V_{i-1_{pu}} V_{i_{pu}} \cos(\delta_i) - 2V_{N_{pu}} V_{1_{pu}} \cos(\delta_1) \tag{15}$$

Labelling DAB1 phase shift angle (δ_1) as a generic control variable (a), i.e., $\delta_1 = a$, and substituting in port power equation (12), then the phase shift angles of the other DABs can be calculated from (16).

$$\delta_i = \sin^{-1}\left(\frac{\sum_{j=1}^{i-1} P_{j_{pu}} + V_{1_{pu}} V_{N_{pu}} \sin(a)}{V_{i_{pu}} V_{i-1_{pu}}}\right) \tag{16}$$

where $i = 2, 3, \ldots N$. By substituting (16) in (15), The square of the total per-unit RMS current formula of the RCDAB topology in terms of (a) is given by (17), as shown at the bottom of the next page.

To minimize the total RMS current, the first derivative of (17) with respect to the main control variable (a) is equated to zero (18), as shown at the bottom of the next page. By solving (18), the optimum value of (a) can be determined and the corresponding phase shift angles of other DAB converters can be determined by (16).

Bisection iterative method for solving nonlinear equations [39] is adopted in this paper to solve equation (18) and find the optimum operating point. Bisection method is initialized with boundaries of the interval in which the solution exists and then converges to the solution with each iteration. The main advantage of this method is that the solution convergence is guaranteed which ensures a stable and optimum operation of the converter.

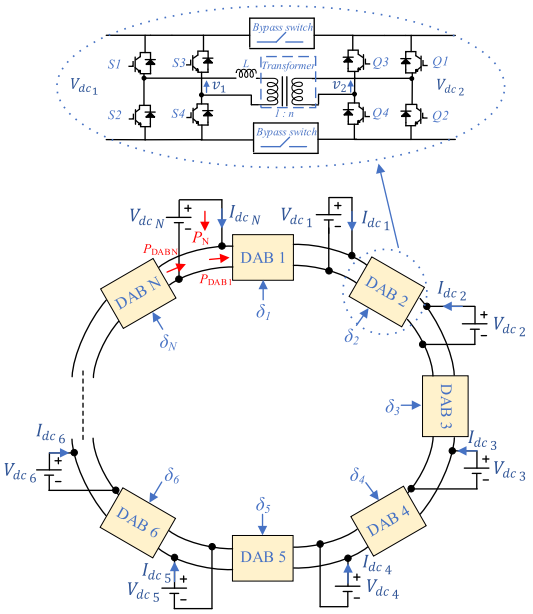

FIGURE 4. The proposed RCDAB topology.

B. RCDAB CONTROLLER

Closed-loop control is applied on the RCDAB topology, where the controller of the RCDAB topology is depicted in FIGURE 5. It is worth noting that in the proposed controller, the N^{th} port is considered to be connected to the main supply, which will supply/absorb the net power to the rest of the ports.

Regarding the other ones, the reference power of each port is subtracted from the actual power value to generate the error signal, which is then being fed to PI controllers

to generate N-1 ports' powers that are fed to the control algorithm. The optimization algorithm needs only N-1 ports' powers to calculate the optimum operating point (phase shift angles) of each of the N DABs (δ_i), where it considers that the last port will achieve the net power. The control algorithm, also, needs the AC RMS voltages that are calculated from the DC voltage of each port. Moreover, an EV connection indicator is applied to each port to detect the idle state of the ports in the optimization algorithm.

The control algorithm is depicted in the flow chart of FIGURE 6, which can be divided into two main control sections: a smart power router (SPR) and an optimization algorithm. The main function of the SPR is to eliminate any unnecessary power processing stages in case there are idle ports, where no supply or battery is connected to the port, only DABs that correspond to the connected ports are enabled, while the remaining DABs are bypassed using the bypass switches, for example, if port 1 is connected then DAB 1 is enabled and so on. Moreover, only the voltages and powers corresponding to the connected ports are considered in the optimization algorithm, where N in (16), (17), and (18) represents the number of connected ports.

It is worth mentioning that the bypass switches open before an EV is connected to the idle port to prevent any inrush current between two ports.

Also, a fault detection occurs in this stage, where if a port voltage is decreased below 0.7 pu or the DC current increases above 1.2 pu, then the two corresponding DABs to the faulted port are disabled (all the switches gating are inhibited).

The next control section is the optimization algorithm, which initiates its action by a feasibility check of available solutions to ensure a more stable controller operation. the algorithm will substitute by the whole range of (a) from $-90°$ to $90°$ in (16) for all DABs. Since DABs are designed to a rated power operation of 1pu, the algorithm checks if the available solutions violate this condition and operate on the nearest feasible solution which increases the stability of the controller. In other words, if feasible solutions are found, the algorithm continues to the next step, and if no feasible solutions are found, the power of the maximum port power is decreased by 1 percent until a feasible solution is found.

Then the optimization algorithm starts its calculations which is based on Bisection iterative method for solving the nonlinear equation (18) to find the optimum solution (phase shift angles for each DAB as mentioned earlier). The algorithm searches for the two successive feasible solutions, where ($I^{2'}_{L_{pu_{total}}}$) changes its polarity. Hence the optimum solution lies between these two successive solutions. Then, the algorithm calculates the mean of the two solutions and replace one of them by their mean value depending on the polarity of the resultant ($I^{2'}_{L_{pu_{total}}}$). The algorithm repeats this cycle until the difference between the two solutions becomes smaller than 1e-3 or the algorithm exceeds 10 iterations. Then the optimum value of a is considered as a_p and optimum phase shift angles of the enabled DABs are calculated by substituting in (16).

IV. STEADY STATE ANALYSIS

To further understand the capabilities and limitations of the RCDAB converter, steady state analysis is performed to estimate converter losses and power flow capability, where unity voltage conversion ratios is assumed (all voltages are equal to their base values).

A. LOSSES ESTIMATION

Converter losses are split into switching losses and conduction losses. However, the switching losses will not be considered in the loss comparison here because zero-voltage-switching occurs at unity conversion ratios which DABs are generally designed for to minimize circulated power [40].

The conduction losses of each H-bridge can be divided into two components: firstly, losses due to parasitic resistances (R_p) that are proportional to the RMS current square. The RMS current can be calculated as in (10). Secondly, losses due to the on-state voltage (V_{on}) of the involved semiconductors (IGBT and diode) that are proportional to the mean of the rectified current which can be calculated as in (19) by substituting with the current in (10).

$$I_{L_{ipu_{av}}} = \frac{2\sqrt{2}}{\pi} \left| I_{L_{ipu}} \right| \tag{19}$$

The total RMS current is calculated as in (20) by substituting by (10).

$$I_{L_{pu_{total}}} = \sqrt{\sum_{i=1}^{N} I^2_{L_{ipu}}} \tag{20}$$

$$I^2_{L_{pu_{total}}} = 2\sum_{i=1}^{i=N} {V_{i_{pu}}}^2 - 2\sum_{i=2}^{i=N} V_{i-1_{pu}} V_{i_{pu}} \sqrt{1 - \left(\frac{\sum_{j=1}^{i-1} P_{j_{pu}} + V_{1_{pu}} V_{N_{pu}} \sin(a)}{V_{i_{pu}} V_{i-1_{pu}}} \right)^2} - 2V_{N_{pu}} V_{1_{pu}} \cos(a) \tag{17}$$

$$\frac{dI^2_{L_{pu_{total}}}}{da} = 2V_{N_{pu}} V_{1_{pu}} \sin(a) + \sum_{i=2}^{i=N} \frac{2V_{1_{pu}} V_{N_{pu}} \cos(a) \left(\sum_{j=1}^{i-1} P_{j_{pu}} + V_{1_{pu}} V_{N_{pu}} \sin(a) \right)}{V_{i_{pu}} V_{i-1_{pu}} \sqrt{1 - \left(\frac{B_i + V_{1_{pu}} V_{N_{pu}} \sin(a)}{V_{i_{pu}} V_{i-1_{pu}}} \right)^2}} \tag{18}$$

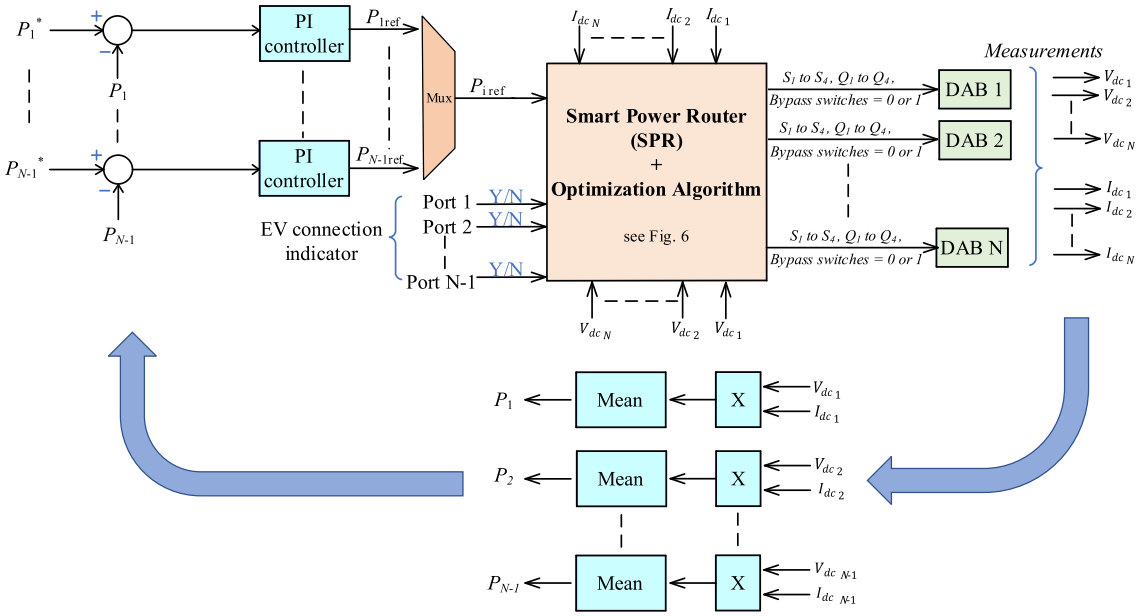

FIGURE 5. The RCDAB topology controller.

On the other hand, the total mean rectified current is calculated as in (21).

$$I_{L_{pu_{av\,total}}} = \sum_{i=1}^{N} I_{L_{ipu_{av}}} \tag{21}$$

Therefore, the total losses in the RCDAB converter can be approximately calculated as in (22) because each DAB is comprised of two H-bridges.

$$P_{l_{RCDAB}} = I^2_{L_{pu_{total\,RCDAB}}} * 2R_p + I_{L_{pu_{av\ total\,RCDAB}}} * 2V_{on} \tag{22}$$

where the efficiency is calculated as follows:

$$Efficiency = \frac{P_{s_{total}} - P_l}{P_{s_{total}}} * 100\% \tag{23}$$

where $P_{s_{total}}$ is the total delivered power while P_l is the losses in the converter.

Assuming a 5-port network with R_p of 50 $m\Omega$ and V_{on} of 1.75 V. Also, it is assumed that two ports are delivering power to the remaining ports, then the efficiency for the RCDAB topology against one of the supplying ports' power is depicted in FIGURE 7. The efficiency is calculated based on (23), where it decreases the as power flow increases. Another case is studied where the power is transferred between only two ports and the remaining ports are disabled and bypassed to eliminate any unnecessary power processing stages as depicted in FIGURE 8. The overall efficiency is, also calculated based on (23) and depicted in FIGURE 9. The efficiency is higher than the previous case because of the bypassed DABs.

B. PORT POWER FLOW CAPABILITY STUDY

The port power delivery capability for the RCDAB topology is calculated based on (12), where the power flow combinations between port i and port $(i+1)$ are shown in FIGURE 10. As port i power increases up to its maximum value of 2 pu, port $(i+1)$ power has a range of applicable combinations from 0 pu down to -2 pu. However, all power flow combinations are possible in the entire power flow range from -2 to 2 pu between two non-adjacent ports. Moreover, the maximum port power is always 2 pu regardless of the number of ports of the multiport converter assuming unity voltage conversion ratios.

V. CONTROL HARDWARE-IN-THE-LOOP VALIDATION

To validate the theoretical claims, a CHiL system has been constructed for a 5-port network using OPAL-RT real-time platform and (DSP) digital signal processing unit shown in FIGURE 11, where the OPAL-RT is based on Intel Core Xeon processor of 4 cores which runs at 3.5 GHz with 16 GB RAM. Port Gigabit Ethernet LAN is used for communication. Nevertheless, the DSP label is TMS320F28335ZJZA with a processor frequency equal to 150 MHz. Besides, the DSP contains the system controller which outputs the firing gates for the IGBTs of the multiport converters built on the OPAL-RT platform.

A nominal DC voltage of 800 V, a base power of 200 kW, and a switching frequency of 1 kHz are used in the CHiL system. The voltage and power ratings are based on a typical EV charging standard CHAdeMO [41].

Assuming unity transformer ratios between all ports, the required base AC inductance is calculated based on (5) and found to be 412.82 μH, where the CHiL system parameters

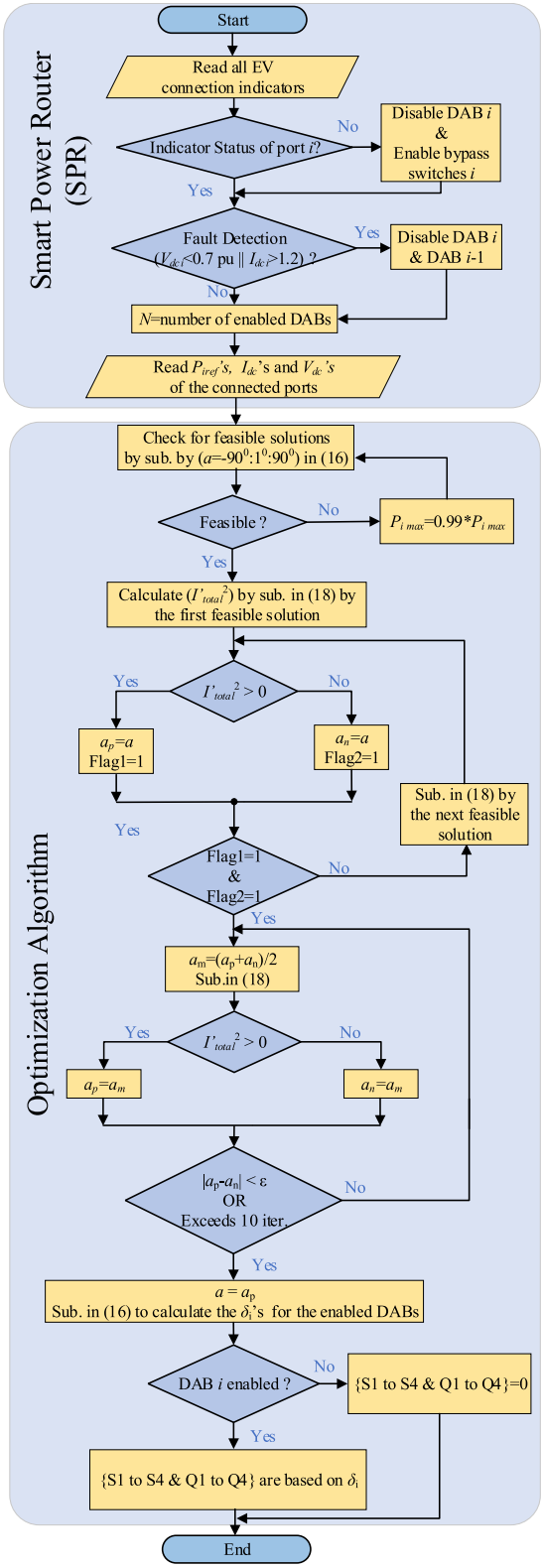

FIGURE 6. Flow chart of the control algorithm containing smart power router (SPR) and optimization algorithm.

are listed in Table 1. The RCDAB topology is tested under different scenarios of normal operation and fault cases to deeply illustrate the behavior of the topology.

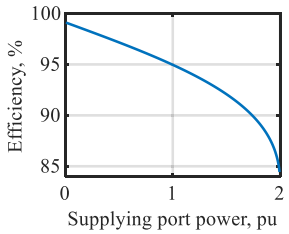

FIGURE 7. Overall efficiency of the proposed RCDAB topology in case of two ports are supplying power to the rest.

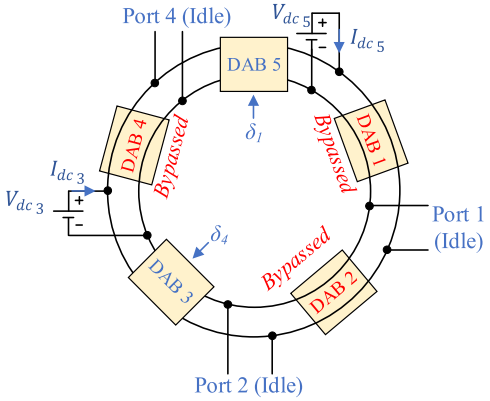

FIGURE 8. The RCDAB topology in the case of only two connected ports while the rest are in an idle state (i.e. open circuit state with no EVs connected).

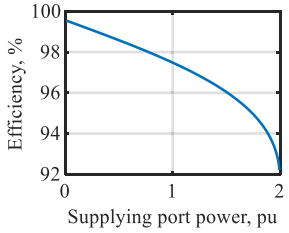

FIGURE 9. Overall efficiency of the proposed RCDAB topology when only two ports are enabled, while the rest are bypassed.

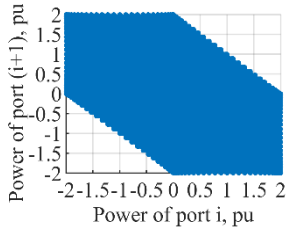

FIGURE 10. Port power delivery of the proposed RCDAB topology (any number of ports).

A. NORMAL OPERATION

The RCDAB topology under ChiL validation is tested in normal operation in three cases. In the first case, the power is delivered from port 2 and port 5 to the remaining ports, while in the second case, the power is transferred between two ports

TABLE 1. CHiL system parameters.

Parameters	Values
DC voltage (V)	800 V
Base voltage (v_{base})	720.25 V
Base power (P_{base})	200 kW
Base current (i_{base})	277.7 A
Base inductance (L_{base})	412.82 µH
Number of ports (N)	5
Inductance per winding (L)	412.82 µH, 50 mΩ
IGBT on-state voltage (V_{on})	1.75 V
Diode on-stage voltage ($V_{d_{on}}$)	1.6 V
Switching frequency (f_s)	1 kHz
Transformers turns ratio (1: n)	1: 1

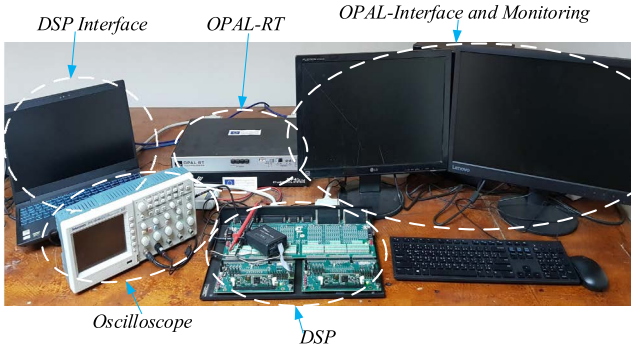

FIGURE 11. CHiL experimental setup.

(port 3 and port 5) only and the rest are in an idle state (open circuit port). In the last case, to test the converters in case of using a varying voltage supply (battery), the voltage of the receiving ports is assumed to be increasing (charging) while the supplying ports deliver constant power.

A closed-loop control is applied for the power flow control which is depicted in FIGURE 5, with the control algorithm depicted in FIGURE 6 to achieve the optimum point operation.

1) FIRST CASE: TWO PORTS SUPPLYING POWER TO OTHER PORTS

In the first case, two ports are supplying power to the remaining three receiving ports at unity voltage conversion ratios, where the variation of the port reference powers in each time-step is shown in Table 2. The active power flow of each port and the corresponding RMS current per DAB are depicted in FIGURE 12(a) and FIGURE 12(b), respectively, where all the ports' powers manage to follow their reference values. Also, it is verified that the power range per port is -2 pu to 2 pu. Moreover, the efficiency of the proposed RCDAB topology can be verified against the theoretical calculation in (23) as shown in FIGURE 12(c).

2) SECOND CASE: POWER TRANSFERRED BETWEEN TWO PORTS ONLY

In the second case study, it is assumed that the power is transferred between two ports only, while the remaining ports are in an idle state. Due to the SPR algorithm, only two DABs are enabled while the rest are bypassed to decrease the number of unnecessary power processing stages as previously

TABLE 2. The reference powers of each port in 4 time steps at unity voltage conversion ratios.

Port number	Power (pu)			
	1st-time step	2nd-time step	3rd-time step	4th-time step
Port 1	-0.8	-0.67	-0.4	-2
Port 2	1.2	1	0.6	2
Port 3	-0.8	-0.67	-0.4	-1
Port 4	-0.8	-0.67	-0.4	-1
Port 5	1.2	1	0.6	2

TABLE 3. The reference powers of each port in 4 time steps at unity voltage conversion ratios.

Port number	Power (pu)			
	1st-time step	2nd-time step	3rd-time step	4th-time step
Port 1	0	0	0	0
Port 2	0	0	0	0
Port 3	-1	-0.7	-0.4	-2
Port 4	0	0	0	0
Port 5	1	0.7	0.4	2

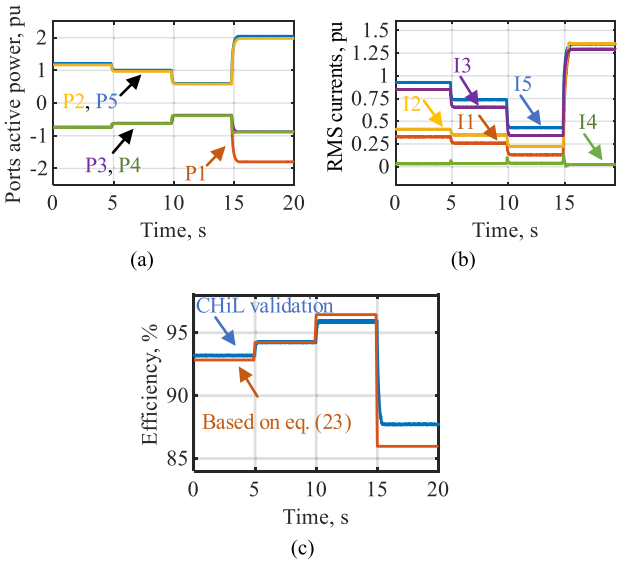

FIGURE 12. Normal operation first case study CHiL results. (a), (b) ports active power and the corresponding RMS currents of each DAB, respectively, and (c)) efficiency of the RCDAB topology.

discussed. Thus, lower losses are achieved which results in higher efficiency of the proposed converter.

The variation of the port reference powers in each time-step is shown in Table 3. The active power flow of each port and the corresponding RMS current per DAB are depicted in FIGURE 13 (a) and FIGURE 13 (b), respectively, where the power is successfully transferred between only two ports. Moreover, FIGURE 13 (c) shows the efficiency of the proposed topology where the efficiency increases by the bypassing operation.

3) THIRD CASE: VARIABLE VOLTAGES (EV BATTERIES CHARGING)

To assess the operation of the proposed topology in case of using variable voltage supplies (EV batteries), where ports 2 and 5 deliver constant power to the remaining ports

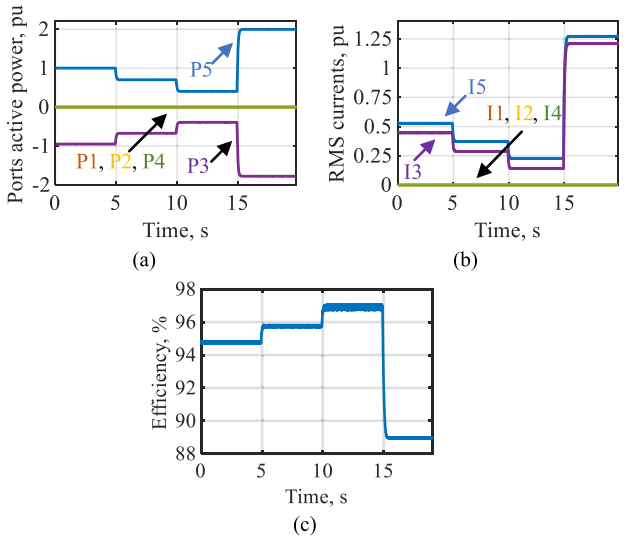

FIGURE 13. Normal operation second case study CHiL results. (a), (b) ports active power and the corresponding RMS currents of each DAB, respectively, and (c) efficiency of the RCDAB topology.

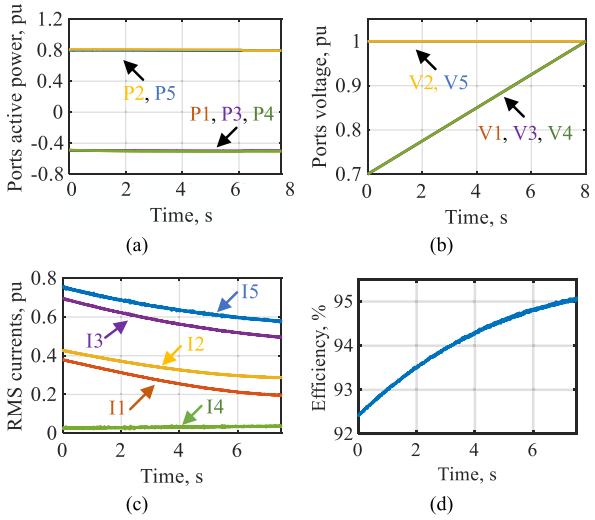

FIGURE 14. Normal operation third case study CHiL results (a) ports active power, (b) voltage profile of each port, (c), (d) RMS currents of each DAB and the efficiency of the RCDAB topology, respectively.

as shown in FIGURE 14 (a), it is assumed that the voltage of the receiving ports is increasing with time (battery charging) according to FIGURE 14 (b). The RMS currents of each DAB and the overall efficiency are shown in FIGURE 14 (c) and FIGURE 14 (d), respectively. It is clear that the RMS currents decreases while increasing the receiving ports voltages, which results in higher efficiency because the optimization algorithm considers the voltage magnitude at each port.

B. OPERATION UNDER FAULTS

Two cases of faults are studied for the proposed topology using CHiL system. Considering the first case, a short circuit fault is applied at one of the receiving ports (to test converter fault tolerance). In the second case, an open circuit fault is applied in one of the H-bridge legs emulating the case of IGBT failing (to test the availability of the converter).

1) FIRST CASE: SHORT CIRCUIT FAULT AT DC PORT SIDE

For the first case, a short circuit fault is applied on port 3 (one of the receiving ports). At the instant of the fault, the faulted port power dropped to zero while the other port powers managed to maintain their values as shown in FIGURE 15 (a) except for the main supply port 5 because it delivers the net power. The ports DC currents are shown in FIGURE 15 (b), where the fault current increases at the instant of the fault. Then after fault detection, the two corresponding DABs are disabled and the fault current decreased to zero.

Since the DC fault current does not exceed the rated value, it is concluded that the proposed topology is fault-tolerant to DC port short circuit faults, with the capability of maintaining power flow to remaining healthy ports.

2) SECOND CASE: OPEN CIRCUIT FAULT IN H-BRIDGE LEG

For the second case, for the RCDAB topology, an open circuit fault is introduced at one of the H-bridge legs in DAB 4. FIGURE 16 (a) shows that at the instant of the fault, the power flow of DAB 3 dropped to zero, while the other DABs change their transferred power in order to compensate for the faulted DAB. Active power is maintained at all ports despite the DAB failure, as shown in FIGURE 16 (b). Therefore, the RCDAB topology succeeds in maintaining port power regulated riding through the open circuit fault. Hence fault-tolerant operation is achieved.

Moreover, for a more detailed explanation of the availability/ fault tolerance of the proposed topology in case of open circuit faults, different scenarios have been addressed as follows, where FIGURE 17 (a) shows a normal power flow operation in the RCDAB topology before any open circuit failure, therefore can be used as a baseline for assessment with the different fault scenarios.

- **Scenario 1:** *RCDAB open circuit failure in one whole DAB unit* (see FIGURE 17 (b)). No power flow interruption at any of the DC ports. Power flow at the DC ports remains the same as the normal operation in FIGURE 17 (a).
- **Scenario 2:** *RCDAB open circuit failure in two different DAB units that are adjacent* (see FIGURE 17(c)). Power flow is interrupted only at one port in between the two adjacent faulted DABs (port 3).
- **Scenario 3:** *RCDAB open circuit failure in two different DAB units that are non-adjacent* (see FIGURE 17(d)). No power flow is interrupted at any DC port.

It is worth noting that the above analysis has shown that the RCDAB will always have at least one more operational DC port during the fault (Scenario 1 and Scenario 2). Scenario 3 has shown that it is yet possible for RCDAB to have all DC ports operational even in the case of two non-adjacent DAB

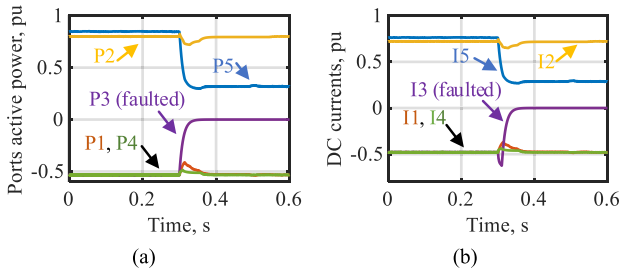

FIGURE 15. CHiL results during a DC port short circuit fault at port 3. (a) ports active power, (b) ports DC current.

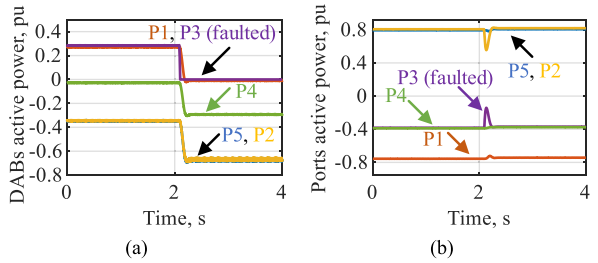

FIGURE 16. CHiL results during an open circuit fault at the H-bridge leg of DAB 3 (a) the active power of each DAB, and (b) the ports active power.

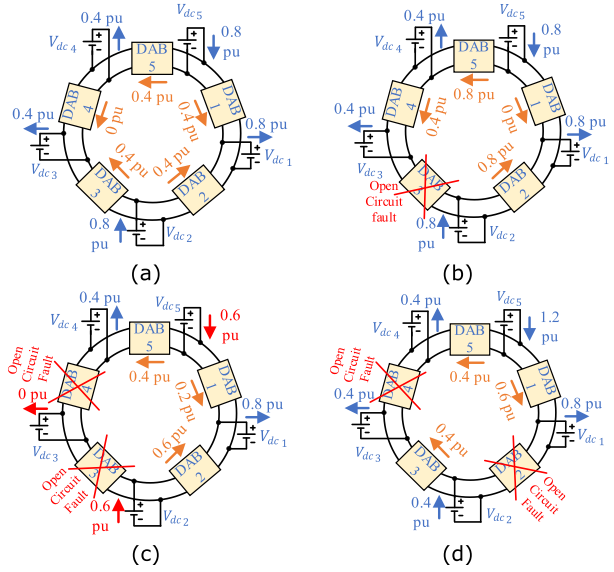

FIGURE 17. (a) normal operation in RCDAB converter without open circuit faults, (b) open-circuit fault in one DAB of RCDAB converter, (c) open-circuit fault in two adjacent DABs of the RCDAB converter, and (d) open-circuit fault in two non-adjacent DABs of the RCDAB converter.

units open circuit faults, depending on the relative positions of the faulted DABs with respect to the supplying and sinking ports.

VI. EXPERIMENTAL HARDWARE VALIDATION

To reinforce the CHiL system results, a simple hardware prototype has been constructed for the RCDAB topology as shown in FIGURE 18 using 3 DABs to provide a 3-port network. A (DSP) digital signal processing unit labelled as

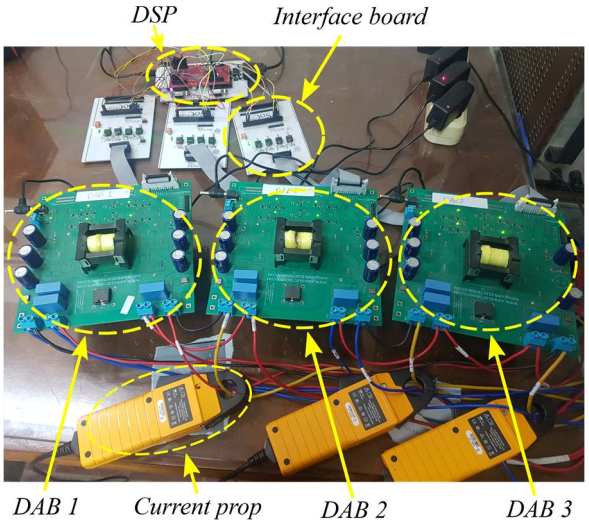

FIGURE 18. The hardware test rig of the RCDAB topology.

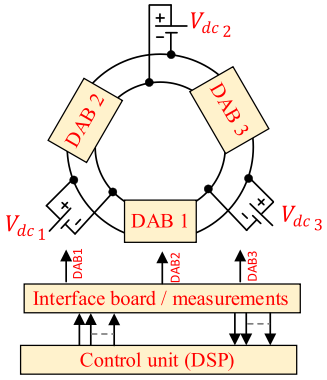

FIGURE 19. The circuit diagram of the hardware test rig.

LAUNCHXL-F28379D with a processor frequency equal to 200 MHz is used as the system controller to generate the suitable firing gates of the multiport converter's switches. The circuit diagram for the constructed test rig is depicted in FIGURE 19. A nominal DC voltage of 24 V, a base power of 200 W, and a switching frequency of 100 kHz are used in the system.

A. NORMAL OPERATION

The system is tested in normal operation in three cases. In the first case, the power is delivered from port 3 to the remaining ports with a step change in the power flow, while in the second case, the power is transferred between two ports (port 1 and port 2) only and the third port is in an idle state (open circuit port). In the last case, to test the converters in case of using a varying voltage supply (battery), the voltage of the receiving ports is assumed to be increasing (charging) while the supplying port delivers a constant power.

The same closed-loop control previously discussed in the paper is applied to the experimental test rig to achieve the desired power flow. Since unity transformer ratios is utilized

TABLE 4. Hardware prototype parameters.

Parameters	Values
DC voltage (V)	24 V
Base voltage (v_{base})	21.6 V
Base power (P_{base})	200 W
Base current (i_{base})	9.26 A
Base inductance (L_{base})	3.7 µH
Number of ports (N)	3
Inductance per winding (L)	3.7 µH
Switching frequency (f_s)	100 kHz
Transformers turns ratio (1: n)	1: 1

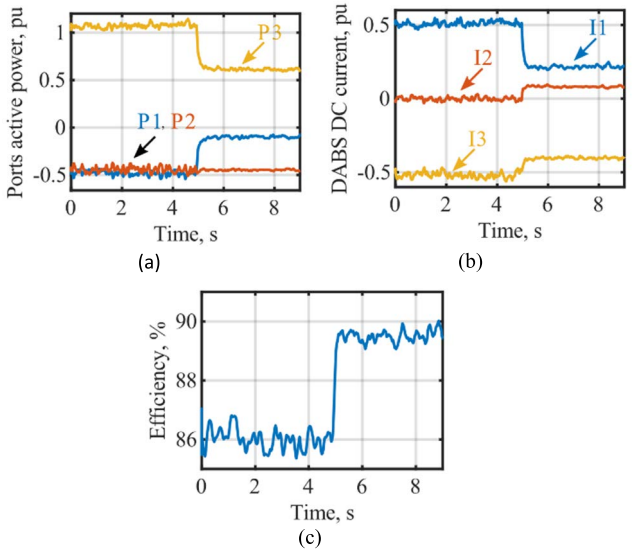

FIGURE 20. Normal operation: first case study hardware results. (a) ports active power, (b) the corresponding DC currents of each DAB, (c) efficiency of the RCDAB converter.

between all ports, the required base AC inductance is calculated based on (5) and found to be 3.7 μH, where the prototype parameters are listed in Table 4.

To clarify the performance of the RCDAB topology, the converters is tested under different scenarios of normal operation and fault cases.

1) FIRST CASE: A STEP CHANGE IN POWER FLOW

In the first case, one port is supplying power to the remaining two receiving ports at unity voltage conversion ratios, where port 1 reference power changes from -0.5 to -0.1 pu, and port 2 reference power maintains its power at -0.5 pu, while port 3 acts as the slack bus which supplies their required power. The active power flow of each port and the corresponding DC current per DAB are depicted in FIGURE 20 (a) and FIGURE 20 (b), respectively. The step change in the power flow occurs at t = 5s. It is obvious that the DC currents of all DABs are changed to achieve the optimum currents at the new power flow combination. Also, the efficiency of the converter is shown in FIGURE 20 (c), where the converter efficiency increases as the power delivered decreases.

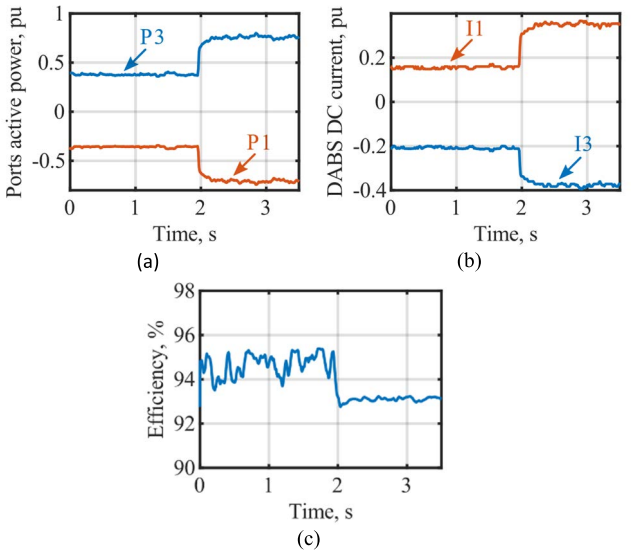

FIGURE 21. Normal operation: second case study hardware results. (a) ports active power, (b) the corresponding DC currents of each DAB, (c) efficiency of the RCDAB converter.

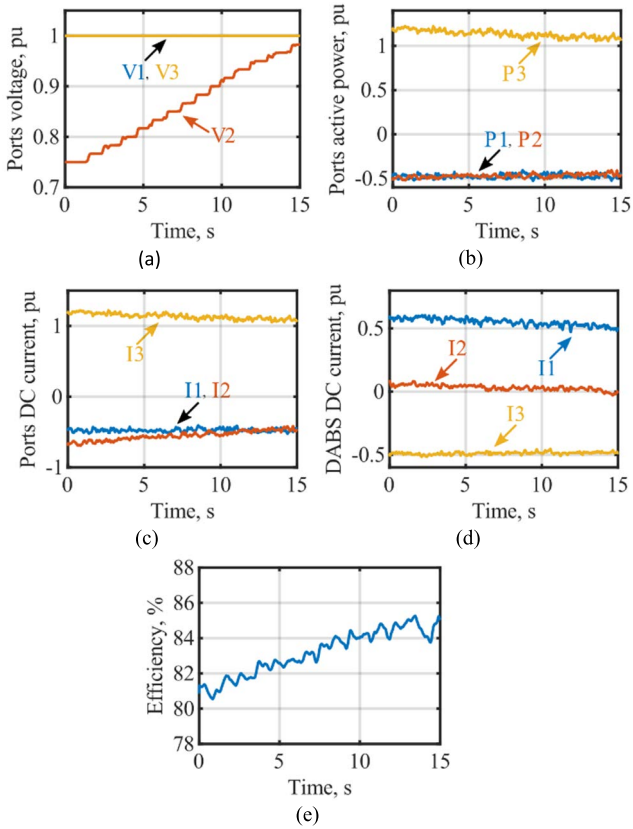

FIGURE 22. Normal operation: third case study hardware results (a) ports voltage profile of each port, (b) ports DC current, (c) ports active power, (d) the corresponding DC currents of each DAB, respectively, (e) efficiency of the RCDAB converter.

2) SECOND CASE: POWER TRANSFERRED BETWEEN TWO PORTS ONLY

In the second case, the power is transferred between two ports only (port 1 and 3) while the remaining port is in an idle state, where port 1 reference power changes from -0.4 to -0.8 pu,

which is supplied from port 3. The active power flow of each port and the corresponding DC current per DAB are depicted in FIGURE 21 (a) and FIGURE 21 (b), respectively, where DAB 2 is successfully bypassed and the power is transferred between two ports only.

Additionally, the efficiency of the converter is depicted in FIGURE 21 (c), where it can be observed that bypassing the DAB 2 increases the converter efficiency.

3) THIRD CASE: VARIABLE DC VOLTAGES SUPPLIES (EV BATTERIES CHARGING)

To test the performance of the topology in case of using variable voltage supplies (EV batteries), it is assumed that the voltage of port 2 is increasing with time (battery charging) according to FIGURE 22 (a). Port 3 delivers constant power to the remaining ports as shown in FIGURE 22 (b). The DC current of each port and the corresponding DC current per DAB are depicted in FIGURE 22 (c) and FIGURE 22 (d), respectively. Since the optimization algorithm in the RCDAB topology considers the voltage magnitude at each port, the DC current of port 2 decreases while increasing its voltage, which results in higher efficiency as depicted in FIGURE 22 (e).

B. OPERATION UNDER FAULTS

The RCDAB topology is tested under different fault scenarios, two cases of faults are studied. In the first case, a short circuit fault is applied at one of the receiving ports, while in the second case, an open fault is applied in one of the H-bridge legs emulating the case of IGBT failing.

1) FIRST CASE: SHORT CIRCUIT FAULT AT DC PORT SIDE

For the first case, a short circuit fault is applied on port 2 (one of the receiving ports). At the instant of the fault the voltage of port 2 dropped to zero as depicted in FIGURE 23 (a), where the DC current of port 2 is increased until fault detection as shown in FIGURE 23 (b). After fault detection, the fault current is decreased to zero. Additionally, the faulted port power dropped to zero while the remaining sinking port power managed to almost maintain its value as shown in FIGURE 23(c). The DAB currents are shown in FIGURE 23(d), where after fault detection, DAB 2 and 3 are disabled to block the fault where their currents are decreased to zero. DAB 1 current is increased to compensate for the dropped DABs.

Since the DC fault current drops to zero, it is concluded that the RCDAB topology is fault-tolerant to DC port short circuit faults, with the capability of maintaining power flow to the remaining healthy ports.

2) SECOND CASE: OPEN CIRCUIT FAULT IN H-BRIDGE LEG

For the second case, an open circuit fault is introduced at one of the H-bridge legs in DAB 2. FIGURE 24(a) shows that at the instant of the fault, the current of DAB 2 dropped to zero, while the other DABs change their transferred power in order to compensate for the faulted DAB. Active power is maintained at all ports despite the DAB failure, as shown in

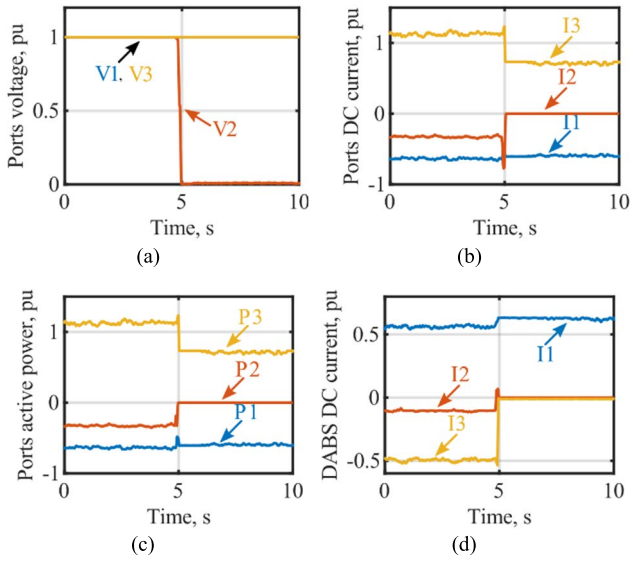

FIGURE 23. DC short circuit fault at port 2 hardware results (a) ports voltage profile of each port, (b) ports DC current, (c), ports active power, (d) the corresponding DC currents of each DAB.

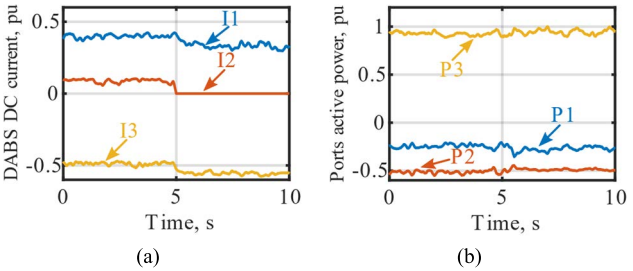

FIGURE 24. Open circuit fault at H-bridge leg of DAB 2 hardware results (a) DC currents of each DAB, (b) ports active power.

FIGURE 24(b). Hence open-circuit fault-tolerant operation is achieved due to the redundant power paths available to the ports through the ring connection of the RCDAB topology.

VII. SUMMARY AND DISCUSSION

This section presents a comparison between different multiport DC-DC topologies that can be used for EV charging stations. The converters taken part in the discussion are the MIPC topology [16], the LCL DC Hub topology [21], the LLC-MWT topology [36], the MAB-MWT topology [32], and the RCDAB topology. The comparison is illustrated in detail in Table 5, which focuses on the features of modularity, DC fault tolerance, availability to open circuit faults, total number of switching devices, feasible power flow solutions and the operation mode of the converter.

It is observed that the RCDAB, the LCL DC Hub and the MIPC converters can be extended to include extra ports hence achieving the feature of modularity. However, only the RCDAB and the LCL DC Hub topologies have the capability of replacing/ eliminating any port without redesigning

TABLE 5. Key feature comparison of DC-DC multiport converters.

Topology	MIPC [16]	LCL DC Hub [21]	LLC-MWT [36]	MAB-MWT [32]	RCDAB
Modularity	Partially Modular	Modular	Non-modular	Non-modular	Modular
DC short circuit fault tolerance	Non-fault tolerant	Fault-tolerant	Fault-tolerant	Fault-tolerant	Fault-tolerant
Redundancy/availability to open circuit faults	Not redundant/Low availability	Not redundant/Low availability	Not redundant/Low availability	Not redundant/Low availability	Redundant/High availability
Total number of switches	$2N$	$4N$	$4N$	$4N$	$8N$
Total number of inductors	$N-1$	$2N$	$2N$	N	N
Total number of capacitors	0	$2N$	N	0	0
Operation mode	Non-resonant	Resonant	Resonant	Non-resonant	Non-resonant
Feasible power flow solutions for a given port power distribution	Only one solution with duty ratio, hence current/loss optimization not possible	Only one solution with SPWM, hence current/loss optimization not possible	Only one solution, hence current/loss optimization not possible	Only one solution with SPS, hence current/loss optimization not possible	Multiple solutions with SPS, hence current/loss optimization possible
Isolation	Non-Isolated	Non-isolated	Isolated	Isolated	Isolated
Control	Duty-Cycle	SPWM	Unregulated	Phase-shift	Phase-shift

the whole converter resulting in full modular multiport converters.

Since most of the topologies are able to endure a short circuit fault applied at any port, these topologies are considered fault-tolerant. But nevertheless, just the RCDAB converter can handle an open circuit fault applied at one of the H-bridge legs due to the redundant power paths through the ring connection of the RCDAB topology. In addition, despite that fact that the number of switches in the RCDAB topology is more than that of the other topologies, the regards about the power losses can be settled by using silicon carbide (SiC) or gallium nitride (GaN) power devices [42].

Also, the RCDAB, the MAB-MWT, and the LCC-MWT are isolated topologies, where the high frequency transformer provides galvanic isolation among the ports and the ability to step up or step down the voltage gain ratio.

Moreover, unlike the rest of the topologies which has only one possible solution for a given power distribution, the RCDAB topology covers a high range of feasible power flow combinations, hence enabling optimization with SPS control, which represents a clear advantage to the RCDAB converter availability in addition to its wider power delivery capability.

VIII. CONCLUSION

A new multiport DC-DC converter has been proposed for electric vehicles' fast-charging stations namely RCDAB topology. Since the RCDAB converter consists of ring-connected DABs with a theoretically infinite number of internal power flow solutions, a novel closed-loop control has been developed to determine the optimal operating point of each DAB that achieves the lowest total RMS current. Also, bypass switches are added to each DAB to eliminate any unnecessary power processing stages in the event of any DC ports being in an idle state with nothing connected to it.

Both CHiL and hardware validations are used in the paper and verified the theoretical claims. Moreover, a comparison has been made between the RCDAB topology and several different multiport converters that are existed in literature, which concludes that although the proposed RCDAB topology has an increased switch count, it provides isolation between the ports with bidirectional capability. It has a fully modular structure that is easily scalable to include additional ports, provides short circuit fault tolerance, open circuit fault tolerance (better availability due to redundant paths for power flow to/from each port). The RCDAB is a promising topology for multiport DC-DC converters in EV fast-charging stations, given the highly favorable features it has proven.

REFERENCES

[1] S. Srdic and S. Lukic, "Toward extreme fast charging: Challenges and opportunities in directly connecting to medium-voltage line," *IEEE Electrific. Mag.*, vol. 7, no. 1, pp. 22–31, Mar. 2019.
[2] C. Botsford and A. Szczepanek, "Fast charging vs. slow charging: Pros and cons for the new age of electric vehicles," in *Proc. Int. Battery Hybrid Fuel Cell Electr. Vehicle Symp.*, 2009, pp. 1–9.
[3] H. Tu, H. Feng, S. Srdic, and S. Lukic, "Extreme fast charging of electric vehicles: A technology overview," *IEEE Trans. Transport. Electrific.*, vol. 5, no. 4, pp. 861–878, Dec. 2019.
[4] *IEEE Standard Technical Specifications of a DC Quick Charger for Use With Electric Vehicles*, IEEE Standard 2030.1.1-2015, 2016, pp. 1–97.
[5] *IEEE Draft Standard Technical Specifications of a DC Quick and Bi-Directional Charger for Use With Electric Vehicles*, document IEEE P2030.1.1/D1, Feb. 2021, pp. 1–159.
[6] M. Grenier, T. Thiringer, and M. G. H. Aghdam, "Design of on-board charger for plug-in hybrid electric vehicle," in *Proc. 5th IET Int. Conf. Power Electron., Mach. Drives (PEMD)*, 2010, p. 152.

[7] H. Wang, A. Gaillard, and D. Hissel, "A review of DC/DC converter-based electrochemical impedance spectroscopy for fuel cell electric vehicles," *Renew. Energy*, vol. 141, pp. 124–138, Oct. 2019.

[8] H. Tao, A. Kotsopoulos, J. L. Duarte, and M. A. M. Hendrix, "Family of multiport bidirectional DC–DC converters," *IEE Proc.-Electr. Power Appl.*, vol. 153, no. 3, pp. 451–458, May 2006.

[9] A. K. Bhattacharjee, N. Kutkut, and I. Batarseh, "Review of multiport converters for solar and energy storage integration," *IEEE Trans. Power Electron.*, vol. 34, no. 2, pp. 1431–1445, Feb. 2019.

[10] H. Zhu, D. Zhang, B. Zhang, and Z. Zhou, "A nonisolated three-port DC–DC converter and three-domain control method for PV-battery power systems," *IEEE Trans. Ind. Electron.*, vol. 62, no. 8, pp. 4937–4947, Aug. 2015.

[11] F. Nejabatkhah, S. Danyali, S. H. Hosseini, M. Sabahi, and S. M. Niapour, "Modeling and control of a new three-input DC–DC boost converter for hybrid PV/FC/battery power system," *IEEE Trans. Power Electron.*, vol. 27, no. 5, pp. 2309–2324, May 2012.

[12] R. Faraji and H. Farzanehfard, "Fully soft-switched multiport DC–DC converter with high integration," *IEEE Trans. Power Electron.*, vol. 36, no. 2, pp. 1901–1908, Feb. 2021.

[13] M. Zhang, Y. Xing, H. Wu, Y. Lu, and K. Sun, "Performance evaluation of a non-isolated bidirectional three-port power converter for energy storage applications," in *Proc. IEEE 8th Int. Power Electron. Motion Control Conf. (IPEMC-ECCE Asia)*, May 2016, pp. 2703–2708.

[14] M. McDonough, "Integration of inductively coupled power transfer and hybrid energy storage system: A multiport power electronics interface for battery-powered electric vehicles," *IEEE Trans. Power Electron.*, vol. 30, no. 11, pp. 6423–6433, Nov. 2017.

[15] M. Amirabadi, H. A. Toliyat, and W. C. Alexander, "A multiport AC link PV inverter with reduced size and weight for stand-alone application," *IEEE Trans. Ind. Appl.*, vol. 49, no. 5, pp. 2217–2228, Sep./Oct. 2013.

[16] A. Hintz, U. R. Prasanna, and K. Rajashekara, "Novel modular multiple-input bidirectional DC–DC power converter (MIPC) for HEV/FCV application," *IEEE Trans. Ind. Electron.*, vol. 62, no. 5, pp. 3163–3172, May 2015.

[17] J. M. Shen, H. L. Jou, and J. C. Wu, "Transformer-less three-port grid-connected power converter for distribution power generation system with dual renewable energy sources," *IET Power Electron.*, vol. 5, no. 4, pp. 501–509, Apr. 2012.

[18] S. Rezaee and E. Farjah, "A DC–DC multiport module for integrating plug-in electric vehicles in a parking lot: Topology and operation," *IEEE Trans. Power Electron.*, vol. 29, no. 11, pp. 5688–5695, Nov. 2014.

[19] T. Kim and S. Kwak, "Single pole switch leg based multi-port converter with an energy storage," *IET Power Electron.*, vol. 9, no. 6, pp. 1322–1330, May 2016.

[20] T. Cheng, D. D.-C. Lu, and L. Qin, "Non-isolated single-inductor DC/DC converter with fully reconfigurable structure for renewable energy applications," *IEEE Trans. Circuits Syst. II, Exp. Briefs*, vol. 65, no. 3, pp. 351–355, Mar. 2018.

[21] D. Jovcic and W. Lin, "Multiport high-power LCL DC hub for use in DC transmission grids," *IEEE Trans. Power Del.*, vol. 29, no. 2, pp. 760–768, Apr. 2014.

[22] J. Zeng, W. Qiao, L. Qu, and Y. Jiao, "An isolated multiport DC–DC converter for simultaneous power management of multiple different renewable energy sources," *IEEE J. Emerg. Sel. Topics Power Electron.*, vol. 2, no. 1, pp. 70–78, Mar. 2014.

[23] Y. Hu, W. Xiao, W. Cao, B. Ji, and D. J. Morrow, "Three-port DC–DC converter for stand-alone photovoltaic systems," *IEEE Trans. Power Electron.*, vol. 30, no. 6, pp. 3068–3076, Jun. 2015.

[24] M. C. Mira, Z. Zhang, A. Knott, and M. A. E. Andersen, "Analysis, design, modeling, and control of an interleaved-boost full-bridge three-port converter for hybrid renewable energy systems," *IEEE Trans. Power Electron.*, vol. 32, no. 2, pp. 1138–1155, Feb. 2017.

[25] M. C. Mira, Z. Zhang, A. Knott, and M. A. E. Andersen, "Analysis, design, modeling, and control of an interleaved-boost full-bridge three-port converter for hybrid renewable energy systems," *IEEE Trans. Power Electron.*, vol. 32, no. 2, pp. 1138–1155, Feb. 2017.

[26] E. Asa, K. Colak, M. Bojarski, and D. Czarkowski, "Asymmetrical duty-cycle and phase-shift control of a novel multiport CLL resonant converter," *IEEE J. Emerg. Sel. Topics Power Electron.*, vol. 3, no. 4, pp. 1122–1131, Dec. 2015.

[27] V. N. S. R. Jakka, A. Shukla, and G. D. Demetriades, "Dual-transformer-based asymmetrical triple-port active bridge (DT-ATAB) isolated DC–DC converter," *IEEE Trans. Ind. Electron.*, vol. 64, no. 6, pp. 4549–4560, Jun. 2017.

[28] T. Pereira, F. Hoffmann, R. Zhu, and M. Liserre, "A comprehensive assessment of multiwinding transformer-based DC–DC converters," *IEEE Trans. Power Electron.*, vol. 36, no. 9, pp. 10020–10036, Sep. 2021.

[29] L. Wang, Z. Wang, and H. Li, "Asymmetrical duty cycle control and decoupled power flow design of a three-port bidirectional DC–DC converter for fuel cell vehicle application," *IEEE Trans. Power Electron.*, vol. 27, no. 2, pp. 891–904, Feb. 2012.

[30] C. Zhao, S. D. Round, and J. W. Kolar, "An isolated three-port bidirectional DC–DC converter with decoupled power flow management," *IEEE Trans. Power Electron.*, vol. 23, no. 5, pp. 2443–2453, Sep. 2008.

[31] J. L. Duarte, M. Hendrix, and M. G. Simoes, "Three-port bidirectional converter for hybrid fuel cell systems," *IEEE Trans. Power Electron.*, vol. 22, no. 2, pp. 480–487, Mar. 2007.

[32] S. Falcones, R. Ayyanar, and X. Mao, "A DC–DC multiport-converter-based solid-state transformer integrating distributed generation and storage," *IEEE Trans. Power Electron.*, vol. 28, no. 5, pp. 2192–2203, May 2013.

[33] L. F. Costa, G. Buticchi, and M. Liserre, "Quad-active-bridge DC–DC converter as cross-link for medium-voltage modular inverters," *IEEE Trans. Ind. Appl.*, vol. 53, no. 2, pp. 1243–1253, Mar. 2017.

[34] G. Buticchi, M. Andresen, M. Wutti, and M. Liserre, "Lifetime-based power routing of a quadruple active bridge DC/DC converter," *IEEE Trans. Power Electron.*, vol. 32, no. 11, pp. 8892–8903, Nov. 2017.

[35] N. D. Dao, D.-C. Lee, and Q. D. Phan, "High-efficiency SiC-based isolated three-port DC/DC converters for hybrid charging stations," *IEEE Trans. Power Electron.*, vol. 35, no. 10, pp. 10455–10465, Oct. 2020.

[36] K. Tomas-Manez, Z. Zhang, and Z. Ouyang, "Multi-port isolated LLC resonant converter for distributed energy generation with energy storage," in *Proc. IEEE Energy Convers. Congr. Expo. (ECCE)*, Oct. 2017, pp. 2219–2226.

[37] N. A. Dung, H. Chiu, J. Lin, Y. Hsieh, and Y. Liu, "Efficiency optimisation of ZVS isolated bidirectional DAB converters," *IET Power Electron.*, vol. 11, no. 8, pp. 1499–1506, Jul. 2018.

[38] S. Shao, L. Chen, Z. Shan, F. Gao, H. Chen, D. Sha, and T. Dragičević, "Modeling and advanced control of dual-active-bridge DC–DC converters: A review," *IEEE Trans. Power Electron.*, vol. 37, no. 2, pp. 1524–1547, Feb. 2022.

[39] A. Eiger, K. Sikorski, and F. Stenger, "A bisection method for systems of nonlinear equations," *ACM Trans. Math. Softw.*, vol. 10, no. 4, pp. 367–377, 1984.

[40] B. Liu, P. Davari, and F. Blaabjerg, "An optimized hybrid modulation scheme for reducing conduction losses in dual active bridge converters," *IEEE J. Emerg. Sel. Topics Power Electron.*, vol. 9, no. 1, pp. 921–936, Feb. 2021.

[41] *Plugs, Socket-Outlets and Couplers for Industrial and Similar Applications, and for Electric Vehicles—Part 1: General Requirements*, Standard IEC 62196, 2014.

[42] B. Zhao, S. Qiang, W. Liu, and Y. Sun, "Overview of dual-active-bridge isolated bidirectional DC–DC converter for high-frequency-link power-conversion system," *IEEE Trans. Power Electron.*, vol. 29, no. 8, pp. 4091–4106, Aug. 2014.

YOUSEF NAZIH received the B.Sc. and M.Sc. degrees in electrical engineering from Alexandria University, Alexandria, Egypt, in 2018 and 2021, respectively. He is currently an Assistant Lecturer with the Electrical Department, Faculty of Engineering, Alexandria University. His current research interests include power electronics, applications of power electronics in power systems, and HVDC systems.

MOHAMED G. ABDEL-MONEIM received the B.Sc. degree in electrical engineering from Alexandria University, Alexandria, Egypt, in 2021. He is currently a Teaching Assistant with the Electrical Engineering Department, Faculty of Engineering, Alexandria University. His research interests include power electronics, battery chargers, and electric vehicles.

AHMED A. ABOUSHADY (Senior Member, IEEE) received the B.Sc. (Hons.) and M.Sc. degrees in electrical and control engineering from the Arab Academy for Science and Technology, Egypt, in 2005 and 2008, respectively, and the Ph.D. degree in power electronics form the University of Strathclyde, U.K., in 2013. He is currently a Senior Lecturer of power electronic systems with Glasgow Caledonian University, U.K. He has numerous publications in refereed journals/conferences and a published textbook, a book chapter contribution, and a PCT patent No. PCT/GB2017/051364. His research interests include dc–dc converters, high-voltage dc transmission systems, grid integration of renewable energy, and distributed generation systems. He is an Associate Editor of IEEE Access.

AYMAN S. ABDEL-KHALIK (Senior Member, IEEE) received the B.Sc. and M.Sc. degrees in electrical engineering from Alexandria University, Alexandria, Egypt, in 2001 and 2004, respectively, and the Ph.D. degree in electrical engineering from Alexandria University and Strathclyde University, Glasgow, U.K., in 2009, under a dual channel program. He has been an Academic Visitor at University of Strathclyde, since March 2021. He is currently a Professor with the Electrical Engineering Department, Faculty of Engineering, Alexandria University. He is an Associate Editor of IEEE Transactions on Industrial Electronics and *IET Electric Power Applications Journal*. He is the Editor-in-Chief of *Alexandria Engineering Journal*. His current research interests include electrical machine design and modeling, electric drives, energy conversion, and renewable energy.

MOSTAFA S. HAMAD (Senior Member, IEEE) received the B.Sc. and M.Sc. degrees in electrical engineering from Alexandria University, Alexandria, Egypt, in 1999 and 2003, respectively, and the Ph.D. degree in electrical engineering from Strathclyde University, Glasgow, U.K., in 2009. He is currently a Professor with the Department of Electrical and Control Engineering, College of Engineering and Technology, Arab Academy for Science, Technology and Maritime Transport (AASTMT), Alexandria. His research interests include power electronics applications in power quality, electric drives, distributed generation, HVDC transmission systems, and renewable energy.